MDPI

*Article*

# Improving Mechanical and Corrosion Behavior of 5052 Aluminum Alloy Processed by Cyclic Extrusion Compression

Jianxin Wu [1], Faramarz Djavanroodi [2,3], Mahmoud Shamsborhan [4], Shokouh Attarilar [5] and Mahmoud Ebrahimi [5,*]

1 Collaborative Innovation Center of Steel Technology, University of Science and Technology Beijing, Beijing 100083, China; wujx9@126.com
2 Department of Mechanical Engineering, College of Engineering, Prince Mohammad Bin Fahd University, P.O. Box 1664, Al Khobar 31952, Saudi Arabia; f.djavanroodi@ic.ac.uk
3 Department of Mechanical Engineering, Imperial College London, London SW7 2AZ, UK
4 Department of Mechanical Engineering, University of Zakho, Kurdistan Region 42001, Iraq; m.shamsborhan@gmail.com
5 National Engineering Research Center of Light Alloy Net Forming and Key State Laboratory of Metal Matrix Composites, School of Materials Science and Engineering, Shanghai Jiao Tong University, Shanghai 200240, China; sh.attarilar@yahoo.com
* Correspondence: mahebr2000@yahoo.com; Tel.: +98-914-401-7268

**Abstract: Background** The severe plastic deformation approach and its well-known cyclic extrusion compression (CEC) method have been established as a powerful tool for fabricating bulk ultrafine-grained metals and alloys with improved properties. **Objective** This study focused on the microstructure evolution, hardness behavior, and corrosion properties of the CEC-processed Al5052 up to four passes compared to the initial annealed state. **Methods** The initial and CEC-processed Al5052 samples at different pass numbers were examined experimentally by EBSD analyses, hardness measurements, and corrosion resistance. **Results** Substantial grain refinement was attained from ~23 μm for the annealed sample to ~0.8 μm in the four passes sample. In addition, the hardness values considerably increased up to 75.7% after four passes from the initial value of 80 HV. In addition, the increment of pass numbers led to a more uniform dispersion of hardness values. Furthermore, the production of more stable protective oxide layers on the UFG structure of the CEC-processed sample led to the improvement in electrochemical response with a corrosion rate reduction from 1.49 to 1.02 mpy, respectively, in the annealed and final pass CEC-processed samples. In fact, the annealed sample manifested more large-sized and deeper pits than the CECed samples due to the increment of potential values and electrochemical attack of chlorine ions that finally deteriorates the corrosion performance. **Conclusions** CEC is an efficient method to improve the mechanical properties of materials due to substantial microstructural changes along with enhancement of electrochemical behavior because of the presence of small-sized and shallow pits.

**Keywords:** severe plastic deformation; Al5052; microstructure refinement; hardness behavior; electrochemical measurement

## 1. Introduction

Reducing energy consumption and air pollution in the automotive industry has become a global challenge over the last decade due to its growing demand. In this regard, the tendency to reduce weight in the used materials is very substantial to increase fuel efficiency and reduce vehicle emissions. In other words, the use of high-strength lightweight materials has become inevitable in today's world [1,2]. It is estimated that an approximate 8–10% increase in fuel efficiency is attained through a 10% reduction in vehicle weight. Accordingly, aluminum (the most abundant metal on the earth) and its alloys, due to their specific properties such as high strength-to-weight ratio, optimal ductility, favorable

corrosion resistance, and recycling potential, have been highly noticed by researchers [2–5]. This has led to the replacement of conventional steel and cast iron with processed aluminum alloys, especially in the vehicles' body panels. Currently, aluminum alloys are widely used in the automobile and aerospace industries. In this regard, 5000 aluminum alloys (Al5000) are utilized comprehensively in the interior panels due to their suitable ductility and formability [6]. However, the safety of the body structure in vehicle accidents has to be considered carefully due to the low strength of the used materials. In this context, grain refinement and the related processes may be an optimal option from the industrial point of view [7]. Note that the Al5000 series, whose main alloying elements are magnesium and manganese, are non-heat-treatable.

The processing methods to fabricate ultrafine-grained (UFG) and even nanostructured metals and alloys have attracted considerable attention due to their enhanced properties in the last three decades. The severe plastic deformation (SPD) technique is one of the substantial approaches for attaining the aforementioned structures in which very large plastic strains, typically in terms of complex stress or high shear state, are imposed on the material without any substantial change in the sample dimensions [8–11]. Until now, numerous SPD methods have been proposed, introduced, and experimented on various materials with different shapes of bulk, sheet, tube, and even wire [12–15]. The most commonly used are equal channel angular pressing [16], high-pressure torsion [17], multi-directional forging [18], equal channel forward extrusion [19], friction stir processing [20], constrained groove pressing [21], accumulative roll bonding [22], planar twist extrusion [23], planar twist channel angular extrusion [24], and cyclic extrusion compression [25].

Cyclic extrusion compression (CEC) as one of the methods of applying severe plastic deformation technique to polycrystalline materials was originated by Richert et al. in 1979 in order to obtain outstanding mechanical properties due to the intensive grain refinement [26]. A schematic illustration of the CEC process is represented in Figure 1. Accordingly, compression simultaneously occurs with the forward extrusion operation in the presence of back pressure during material flow between two chambers of diameter d0 through the connecting channel of diameter dm. Consequently, the sample is restored to its initial shape. By repeating this deformation cycle, high values of plastic strain can be applied without removing a sample from the die between successive passes [27–29]. This is one of the advantages of this method over other SPD techniques, such as equal channel angular pressing and multi-directional forging.



**Figure 1.** Schematic representation of the steps of the cyclic extrusion compression (CEC) process, including (**a**) initial conditions of the die setup; (**b**) the first cycle of extrusion compression deformation, (**c**) 180° inversion of the die, and (**d**) the second cycle of extrusion compression deformation.

As known, plastic deformation in aluminum and other metals and alloys occurs using the slip mechanism along the crystallographic planes in their grains. Aluminum alloys

have 12 slip systems due to the face-centered cubic (fcc) structure, which allows them to accommodate a large amount of plastic deformation, thus increasing their formability. The corresponding slip system is {111} ⟨110⟩. Previous studies have shown that approximately 5% of the deformation energy is stored as internal energy, and the rest is dissipated as heat. Most of this stored energy is strain energy, which is associated with dislocations [30–32]. Note that the number of dislocations always increases during plastic deformation as a result of dislocation multiplication and the formation of new dislocations through grain boundaries, internal defects, and surface irregularities [33].

A review of previous work on the severe plastic deformation methods shows that no study has been conducted so far on the 5052 aluminum alloy by the CEC method. An ultrafine-subgrain structure of the Al5052 alloy after the cold differential speed rolling (DSR) deformation was investigated experimentally by Ko and Hamad [34]. The results indeed demonstrated that the DSR process followed by the annealing at 473 K for 1 h is suited for attaining a combination of enhanced properties of strength (310 MPa) and ductility (~10%) as compared to the initial and deformed samples. Naeini et al. studied the corrosion behavior of UFG Al5052 after processing by ARB using potentiodynamic polarization, cyclic voltammetry, and immersion tests [22]. It was found that increment of ARB pass numbers leads to the deterioration of pitting corrosion resistance that is presumably due to microstructure refinement and defect/dislocation density increase. Incremental rolling at both room and cryogenic temperatures was performed on the ARB-processed Al5052 sheets by Mohebbi and Akbarzadeh [35]. In this regard, several experimental and numerical analyses were carried out to find the deformation parameters that are required to study the evolution of microstructures and mechanical properties. The surface roughness evolution of the Al5052 after processing by surface nanocrystallization and hardening (SNH) was studied experimentally as a function of the processing time and the ball size [36]. The results indicated that the surface roughness can be divided into the roughness increase, roughness decrease, and the steady-state stages. This is due to the relation of the different surface coverage stages by indents induced by the impacting balls during the process. In addition, an analytical model was proposed based on the fully plastic contact theory to anticipate the corresponding surface roughness and finally provide the essential knowledge for optimization of the process to minimize the surface roughness [37]. The ductile fracture behavior of the Al5052 sheet after cyclic plastic deformation is studied by Yagami et al. to determine the deformation consequence on formability enhancement in incremental stretch sheet forming at room temperature [38]. The results indicated that the deformability increases due to the cyclic bending–unbending deformation because of strain distribution and accumulation effects. Microstructural characterization and mechanical properties of Al5052 sheets were analyzed experimentally by Gang et al. during cryogenic rolling followed by warm rolling [39]. The combination of cryogenic rolling with warm rolling at 448K led to considerable tensile strength enhancement up to 452 MPa. In this regard, the formation of fine precipitates during warm rolling is controlled by the diffusion of magnesium in the aluminum matrix. Entezami and Honarpisheh studied the effect of the equal channel angular rolling process up to five passes on the Al5052 hardness behavior [40]. It became evident that the sample hardness was improved by increasing the pass number. In this regard, its value is increased by getting close to the sample surface from the center. The effects of temperature and strain rate during the plastic deformation behavior of Al5052 were investigated by Song et al. through quasi-static tensile and split Hopkinson pressure bar tests [41]. The results indicated that strain rate sensitivity of the alloy is minimal in the range of 0.001 to 3000 $s^{-1}$, while temperature significantly impacts the material plastic behavior.

Based on the authors' knowledge obtained from the literature survey, no comprehensive study has yet been performed on the CEC processing of the Al-Mg alloys. In fact, the mechanical properties and corrosion behavior of CEC-processed Al5052 alloy, which is the main innovation of this research, have not been studied so far. Consequently, this topic still deserves further attention. Accordingly, this investigation dealt with the

feasibility of using the CEC method to impose an intensive shear strain on the highly formable 5052 aluminum alloy up to fracture in order to obtain an ultrafine-grained state. In the following, microstructure evolution, texture components, mechanical properties, and corrosion behavior of the initial (annealed) and CEC-processed Al5052 were compared and discussed comprehensively.

## 2. Materials and Methods

A commercial 5052 aluminum alloy (Al5052), due to its many applications in aircraft, vehicles, marine, general sheet metal forming, architecture, heat exchangers, fuel lines and tanks, rivets, wires, flooring panels, streetlights, and appliances, was utilized in this study. The chemical compositions of this alloy are listed in Table 1, which has been obtained by the optical emission spectroscopy (OES) technique. The mentioned material was annealed at 380 °C for 2 h (according to our previous results [16,21]) and then cooled slowly at the furnace down to room temperature resulting in the most homogeneous equiaxed structure with a mean grain size of ~23 μm that is free of residual stresses. Afterward, the CEC process was performed up to four passes at ambient temperature on the cylindrical shape aluminum samples with a diameter and length of 20 mm and 110 mm, respectively. Note that CEC processing at ambient temperature leads to the most hard-working/strain-hardening on the material. For this aim, a hydraulic pressing machine was applied with a constant velocity of 6 mm/min. In addition, molybdenum disulfide ($MoS_2$) was used as lubrication during the process to minimize frictional effects. It should be noted that the initial and extruded diameters of the CEC die are equal to 20 mm and 16 mm, respectively, in order to obtain an extrusion ratio of $A_0/A_f = 1.56$, where $A_0$ and $A_f$ are the initial and extruded (final) cross-sectional areas. Note that each pass includes two cycles of extruding the sample from 20 mm to 16 mm diameter followed by compression to its initial 20 mm diameter. In this regard, the amount of equivalent plastic strain during the CEC method can be calculated by Equation (1), where $D$, $d$, and $n$ denote the initial diameter, extruded diameter, and pass numbers, respectively [29,42]. The die setup was designed to attain the plastic strain value of about 0.9 in each cycle; this corresponds to the value obtained in the conventional ECAP process for the die channel angle of 90°. Accordingly, the amount of plastic strain at each cycle would be 0.893. Eventually, microstructure evolution, mechanical behavior, and corrosion resistance of the initial (annealed) and CEC-processed samples were examined and investigated.

$$\varepsilon = 4n\frac{D}{d} \tag{1}$$

**Table 1.** Chemical composition (in wt.%) of the studied 5052 aluminum alloy in this work.

| Element | Mg | Fe | Cr | Si | Cu | Zn | Mn | Al |
|---|---|---|---|---|---|---|---|---|
| Composition | 2.73 | 0.42 | 0.27 | 0.24 | 0.14 | 0.14 | 0.12 | Balance |

For characterizing microstructure evolution and texture behavior of aluminum samples before and after the CEC process up to four passes, field-emission scanning electron microscopy (FE-SEM) equipped with electron backscatter diffraction (EBSD) was utilized. For EBSD observation, sample sectioning was mechanically performed, then polished electrolytically in a solution of 30% $HNO_3$ and 70% $CH_3OH$ at the temperature and voltage of about 30 °C and 15 V, respectively. Accordingly, the obtained EBSD data were analyzed using TSL-OIM and ATEX software [43]. Note that evolution of the crystallographic texture was carried out by the measurement of incomplete pole figures of {111}. Moreover, Vickers microhardness tests were carried out on the annealed, the first, second, and final passes of the CEC-processed aluminum samples using a microhardness testing machine (Mitutoyo HM-210/220 Type-D Vickers hardness device) under the applied load and dwell time of 20 g and 10 s in accordance with the ASTM E384. Each test was repeated twice, and its average value was chosen. In this regard, 371 measurements were measured on the 5 mm circular cross-sectional area of each condition after grinding and polishing. In addition,

an average HV magnitude and the related standard deviation in order to measure its distribution uniformity were calculated and compared for each state.

All corrosion tests were carried out in 3.5% sodium chloride (NaCl) solution using the potentiodynamic polarization method at room temperature with a scan rate of 0.8 mV/s from the potential of −400 up to 100 mV SCE after 15 min open-circuit immersion to study the effect CEC processing on the corrosion resistance of Al5052 in detail. It should be mentioned that this test was conducted in accordance with the ASTM G102 on the square-shaped samples with the length and thickness of 10 mm and 1 mm, respectively. For this aim, the surface of all samples was cleaned using acetone in an ultrasonic cleaner and dried in the air before and after the polarization experiment. In addition, all samples were maintained in the testing solution for a while before the experiments to attain the steady-state open-circuit potential. For this type of corrosion test, a typical three-electrode setup was utilized, including a Pt electrode as a counter electrode, a saturated calomel electrode (SCE) as a reference, and an aluminum sample as a working electrode. Note that the standard electrode potential of the calomel electrode in 1 M KCl is 0.28 V. After testing, corrosion potential ($E_{corr}$), corrosion current density ($i_{corr}$), and corrosion rate were extracted from each potentiodynamic curve using the popular procedure of Tafel extrapolation. Each corrosion test was repeated twice, then the corresponding average magnitudes were reported. Eventually, an FEI Quanta-600 SEM was applied to observe the sample surfaces after the polarization examinations.

## 3. Results and Discussion

### 3.1. Microstructure Evolution

Figure 2 represents EBSD analyses of Al5052 alloy before and after the CEC process up to four passes. Note that these images were obtained from the cross-section of the samples. Accordingly, the inverse pole figure (IPF), Kernel average misorientation (*KAM*), and recrystallized grains have been obtained for the first, second, and final passes of the CEC-processed samples and compared with the as-received (annealed) state. IPF results indicate that grain refinement occurs during the CEC process and continues as the pass number increment. The average grain size of ~23 μm for the annealed state is decreased drastically to 6 μm by the processing one pass CEC process. There is also about a 67% reduction at the second pass compared to the first pass. Finally, an average grain size of about 0.8 μm (ranging from 0.4 to 1 μm) is attained for the final pass of the CECed sample, which is a UFG structure. In addition, four passes of the CEC process led to the relatively spherical and equiaxed morphology in most grains. Moreover, the effect of grain refinement at the initial passes is more significant than at the subsequent passes, which is in accordance with relevant references [44,45]. This is maybe related to reducing the stacking fault energy and increasing the twining capacity.

The reason for intensive grain refinement in the CEC process, as one of the main SPD methods, is principally due to the increase in the density of dislocations and the consequent formation of low-angle grain boundaries (LAGBs) at the initial passes. Subsequently, the above-mentioned LAGBs are converted to high-angle grain boundaries (HAGBs) at the higher pass numbers as a result of imposing a large amount of plastic strain. As a result, the alloy with UFG structure and even NS is formed. Furthermore, Table 2 lists the fraction of LAGBs and HAGBs for each Al5052 state shown in Figure 2. Based on this table, it is clear that the annealed state of the alloy has the highest fraction of HAGBs. Applying one pass CEC process decreases the fraction of HAGBs from 89.3% to 58.7%. In this regard, subsequent passes compensate relatively for it, so that its value increases gradually to 76.6% at the fourth pass. Therefore, the four-pass CEC-processed Al5052 alloy has the highest HAGB fraction compared to other deformed conditions.
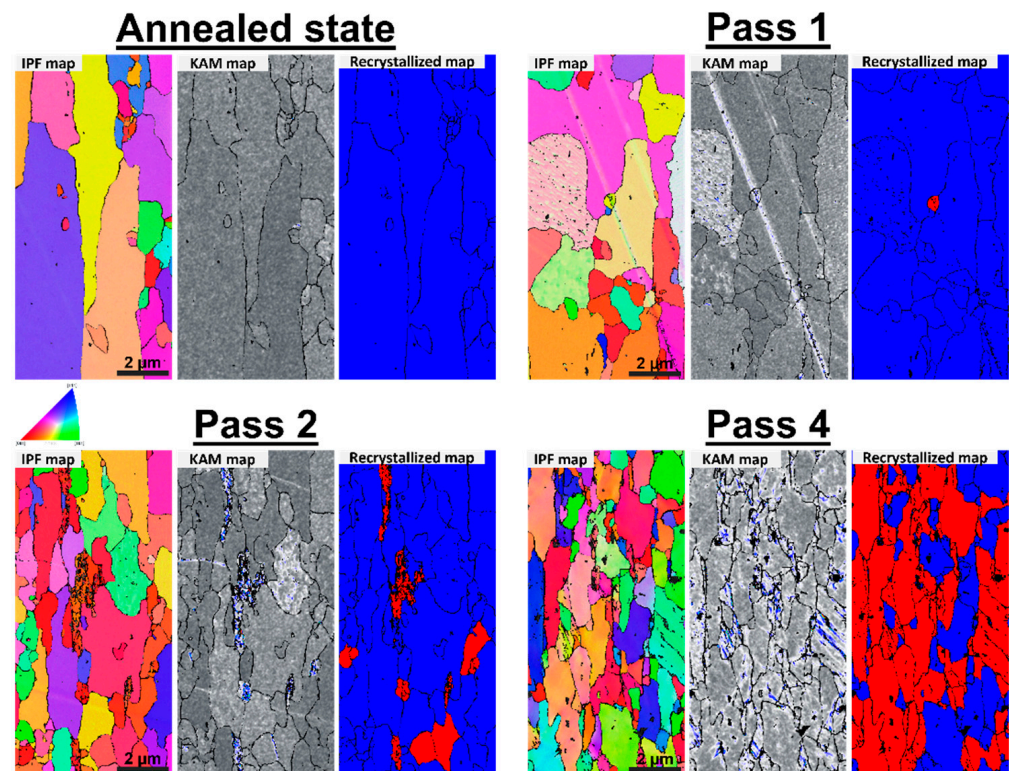
**Figure 2.** Electron backscatter diffraction (EBSD) analysis of Al5052 alloy after the CEC process at room temperature up to four passes. Note that inverse pole figure (IPF), Kernel average misorientation (*KAM*), and recrystallized grains were extracted for the annealed, the first, the second, and the fourth (final) passes, respectively.

**Table 2.** EBSD analysis results in terms of grain boundary length and LAGBs and HAGBs fractions for Al5052 alloy under different CEC processing conditions.

| Material State | Parameters | Grain Boundary Type | |
|---|---|---|---|
| | | LAGBs ($2°$–$15°$) | HAGBs ($>15°$) |
| Annealed state | Fraction (%) | 10.7 | 89.3 |
| | Boundary length in 100 $\mu m^2$ | 5.6 | 53.2 |
| The first pass | Fraction (%) | 41.3 | 58.7 |
| | Boundary length in 100 $\mu m^2$ | 99.6 | 208.9 |
| The second pass | Fraction (%) | 32.8 | 67.2 |
| | Boundary length in 100 $\mu m^2$ | 73.2 | 283.4 |
| The fourth pass | Fraction (%) | 23.4 | 76.6 |
| | Boundary length in 100 $\mu m^2$ | 65.7 | 375.4 |

The increment of HAGBs fraction at the subsequent passes may be related to the occurrence of dynamic recrystallization during the CEC process. In this regard, the recrystallized maps in Figure 2 and the *KAM* map and diagrams in Figures 2 and 3 verify the achieved findings. Previous studies have shown that continuous dynamic recrystallization (CDRX) is the predominant mechanism of dynamic grain refinement in aluminum alloys with high stacking fault energy (SFE) over a wide range of temperatures [31,32,46–48]. In this respect, the dynamic grain refinement rate, which is controlled by the CDRX mechanism, in turn, is intensely dependent on the phase composition of the aluminum alloy and the deformation temperature. However, a complete recrystallization structure occurs only at sufficiently high plastic strain. Note that any reduction in the critical plastic strain imposed on the aluminum alloy is significant for fabricating UFG and even NS conditions. CDRX has been shown to involve the formation of stable 3D arrays of deformed LAGBs,

followed by their gradual conversion to HAGBs after imposing extreme plastic strains through trapping mobile dislocations. Subsequently, new grains are formed as a result of increased sub-boundary misorientation due to the continuous accumulation of dislocations during deformation. This mechanism is fully consistent with the results obtained from this study in Figure 2 and Table 2. On the other hand, the formation of deformed subgrains is the slowest process in aluminum alloys that controls the overall CDRX rate. Therefore, the occurrence of CDRX may be facilitated considerably through the initial deformation bands. Accordingly, geometrically necessary boundaries (GNBs) with initial low-angle misorientation begin to appear at moderate plastic strains, leading to large misorientations. In addition, the subdivision of the original grains into 3D arrays bounded by dislocation boundaries with low-angle misorientation occurs in the following. It is clear that this process plays a significant role in the CDRX initiation at low and intermediate temperatures. This mechanism is called geometric dynamic recrystallization (GDRX) and could be considered an abnormal or apparent CDRX [31,49]. The mentioned mechanism is shown schematically in Figure 4.
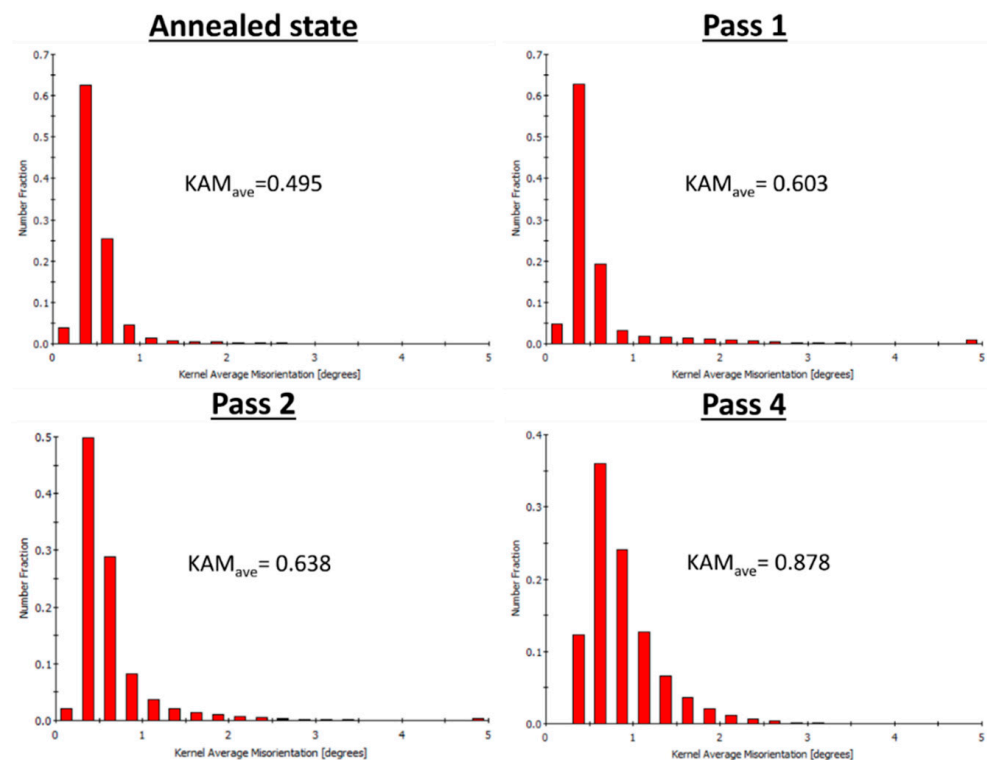


**Figure 3.** Kernel average misorientation (*KAM*) diagram of Al5052 alloy before and after the CEC process at room temperature up to four passes.
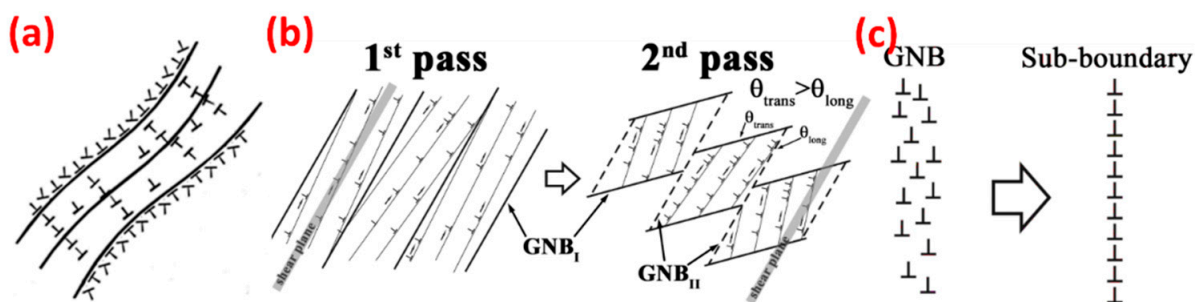


**Figure 4.** Schematic representation of the geometric dynamic recrystallization (GDRX) mechanism, including (**a**) the formation of geometrically necessary boundaries (GNBs), (**b**) the formation of 3D arrays of GNBs, and (**c**) the transformation of a GNBs to a sub-boundaries [31].

To evaluate the dislocation density in Al5052 alloy before and after the CEC process at different pass numbers, Kernel average misorientation (*KAM*) could be an effective method in which the local misorientation is measured using the orientation data in EBSD. As known, local misorientations across the grains are very closely interconnected to the geometrically necessary dislocations (GNDs) that occur due to the adaption of the lattice distortion because of the mismatch of active slip systems between areas adjacent to a grain. Thus, the evolution of GNDs is investigated by measuring the local misorientation of aluminum samples. In this regard, the *KAM* map and its average value for the annealed and CEC-processed Al5052 alloy in Figures 2 and 3 reflect the geometric dislocation density ($\rho$) distribution around the grains. Note that almost all dislocations are concentrated in the broken fine grains. The results showed that the average *KAM* value, which is equal to 0.495 for the initial annealed state, is increased by about 22%, 29%, and 77% after the first, second, and fourth passes, respectively. Equation (2) can be utilized in order to calculate the density of GNDs ($\rho_{ave}$) based on the obtained average *KAM* value ($KAM_{ave}$) [50]. In this relationship, $\mu$ and *c* are step size and the Burgers vector, respectively, which are equal to 0.20 $\mu$m and 0.286 nm for this study. Based on Equation (2), the density of GNDs in the annealed state, the first, the second, and final pass of CEC-processed Al5052 alloy are $1.73 \times 10^{17}$ m$^{-2}$, $2.11 \times 10^{17}$ m$^{-2}$, $2.23 \times 10^{17}$ m$^{-2}$, and $3.07 \times 10^{17}$ m$^{-2}$, respectively. The obtained findings are in suitable agreement with the achieved results in the CDRX mechanism, which is based on the increment of dislocation density due to the CEC application. Both state that the density of dislocations and the degree of deformation are directly related to each other. As the degree of deformation increases, numerous dislocations are generated in the sample, and the density of dislocations increases sharply.

$$\rho_{ave} = \frac{2KAM_{ave}}{\mu b} \tag{2}$$

### 3.2. Hardness Behavior

In this section, the hardness behavior of Al5052 alloy was investigated before and after the CEC process at different passes. For this aim, the average hardness value and hardness distribution at the sample cross-section were obtained and plotted in Figure 5. Note that the polar coordinate system (r, $\theta$, HV) was utilized to draw the observed graphs. In this system, r and $\theta$ change from 0 to 2.5 mm with a step of 0.5 mm and 0 to 360° with a step size of 10°, respectively. Therefore, a total of 371 hardness measurements were recorded, and the corresponding contour plots were drawn using MATLAB software. As is observed, the initial state of aluminum alloy has an average hardness value of 80 HV with the lowest dispersion, which may be related to the annealing operation of samples before processing. By applying one pass of the CEC process, its value increases drastically to 108 HV with relatively high dispersion. This dispersion is the highest value compared to other processed states of the sample. At the second pass CEC-processed sample, the average hardness value reaches 120.6 HV with a lower dispersion than the previous state. In addition, the average hardness value of Al5052 after four CEC passes has its maximum value, which is equal to 139.7. To quantitatively investigate the dispersion of hardness distribution in the above samples, the standard deviation (SD) criterion was calculated and achieved. In statistics, SD measures the amount of variation or dispersion in a set of values. A low standard deviation indicates that the values are close to the average, while a high standard deviation indicates that the values are spread over a wider range. Accordingly, the annealed state Al5052 has an SD value of 0.870, while after the first pass, it increases to 4.339, after the second pass to 3.892, and after the fourth pass to 3.738. As a result, the final pass CEC-processed alloy has the highest hardness value with suitable dispersion uniformity. In addition, the hardness in the central region is the lowest value, which gradually increases with the distance from it and reaches the maximum value in the periphery. This may be due to the application of intense plastic strains, which are related to the friction between the sample and the die in that region.
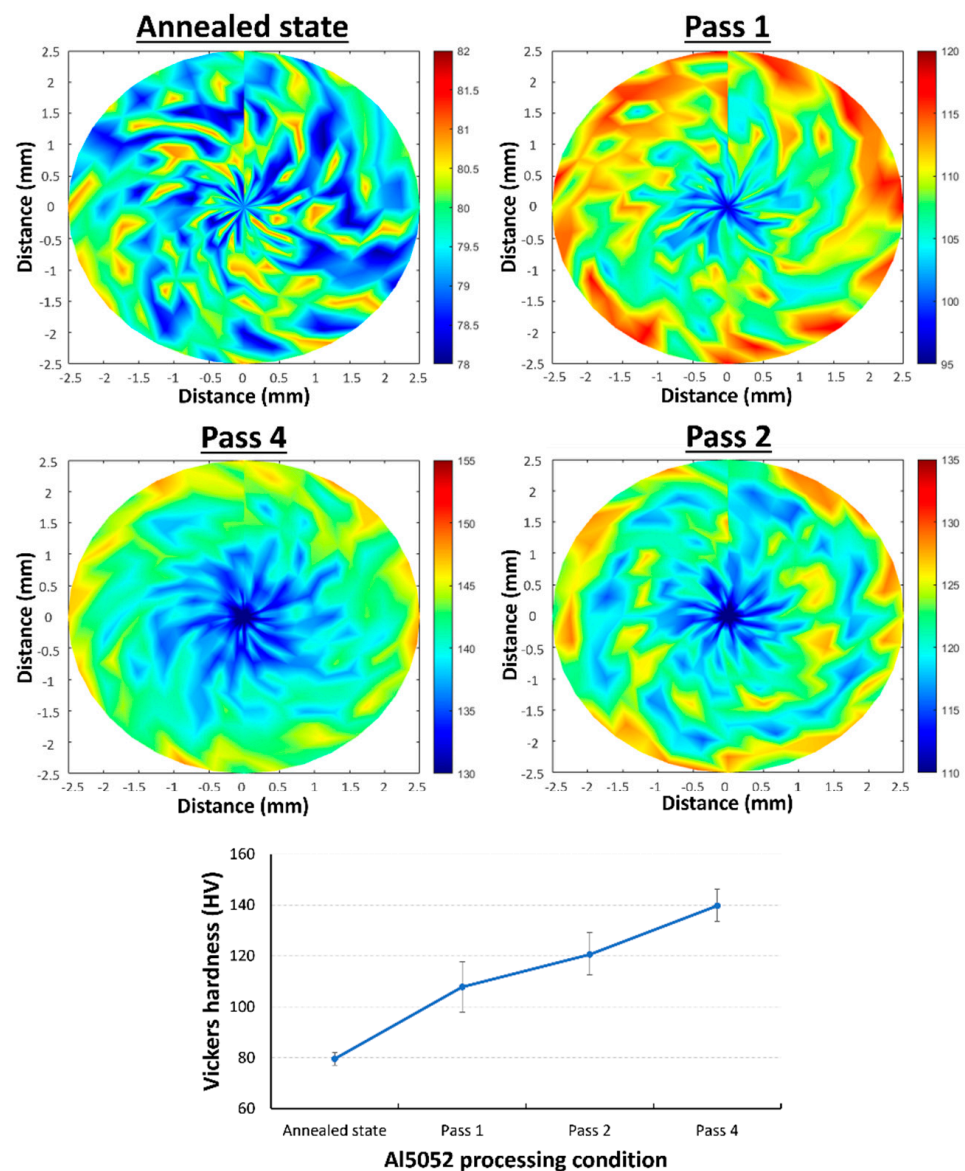
**Figure 5.** Hardness behavior, including average hardness value and its distribution at the cross-section for the Al5052 alloy before and after the CEC process at different pass numbers up to four passes.

### 3.3. Corrosion Resistance

The potentiodynamic polarization curves of the Al5052 alloy before and after the CEC process at different pass numbers (up to four passes) are represented in Figure 6. It can be seen that during the potential increase, the shape of all the curves is almost the same, and no fundamental change is detectable. It means that all samples have passed the active and active-passive transition with increasing potential. Thus, similar electrochemical behavior is observed regardless of the application of the CEC process or pass number. Table 3 lists the salient electrochemical corrosion parameters of the Al5052 samples in different processing conditions according to the obtained curves in order to quantitatively analyze their corrosion behavior. Based on this, the four-pass CEC-processed Al5052 alloy is found to have the best corrosion resistance with a corrosion rate of 1.023 mils penetration per year (mpy) compared to the annealed sample with 1.489 mpy, and the one pass and two pass samples with respective corrosion rates of 1.111 and 1.055 mpy. It indicates that about 25%, 5%, and 3% reductions in the corrosion rate are attained after the first, second, and fourth passes of the CEC process, respectively, compared to the previous state. It can be concluded

that the aluminum sample after plastic deformation manifested a better corrosion behavior than the initial annealed state.
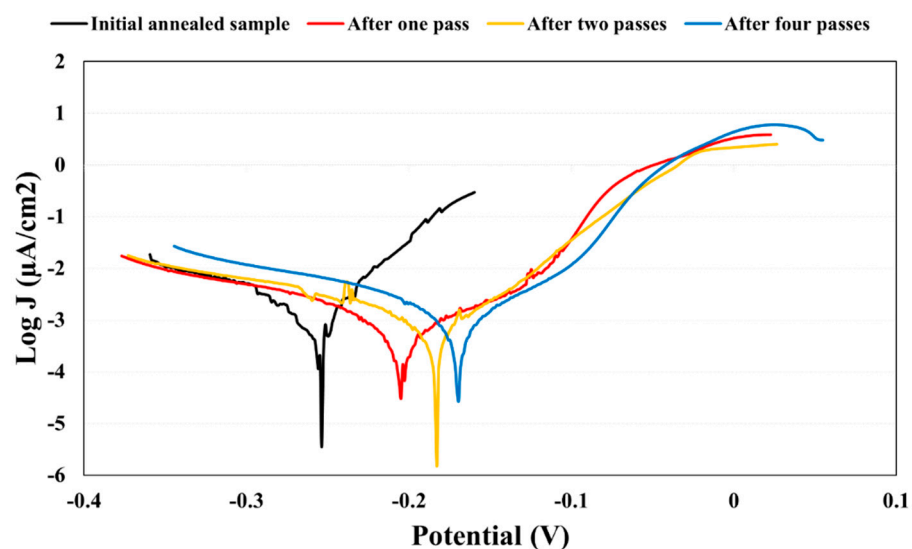


**Figure 6.** Potentiodynamic polarization curve of the Al5052 alloy before and after the CEC process up to four passes.

**Table 3.** Electrochemical corrosion salient parameters in the Al5052 alloy before and after the CEC process up to four passes.

| Sample State | $E_{corr}$ (mV) | $i_{corr}$ ($\mu A/cm^2$) | $B_a$ (R-Squared Value) | $B_c$ (R-Squared Value) | Corrosion Rate (mpy) |
|---|---|---|---|---|---|
| Annealed state | −253.1 | 4.31 | 28.241 ($R^2$ = 0.983) | 12.461 ($R^2$ = 0.896) | 1.489 |
| After the first pass | −204.7 | 3.21 | 20.966 ($R^2$ = 0.963) | 7.6252 ($R^2$ = 0.953) | 1.111 |
| After the second pass | −182.8 | 3.05 | 19.690 ($R^2$ = 0.971) | 6.7071 ($R^2$ = 0.943) | 1.055 |
| After the fourth pass | −169.4 | 2.96 | 21.050 ($R^2$ = 0.951) | 7.5487 ($R^2$ = 0.950) | 1.023 |

It was reported that Al5052 alloy has a favorable corrosion resistance mainly due to the fabrication of a protective surface oxide layer and has a low corrosion rate, especially in saline solutions and marine applications [51]. As it can be inferred from Figure 6, the corrosion resistance of Al5052 alloy is further promoted by the application of the CEC method. In addition, increasing the pass numbers positively changes the corrosion behavior since the application of only one pass of CEC leads to 34% corrosion enhancement, which is reached approximately 45.5% after four passes. This considerable promotion can be related to several reasons such as grain refinement (increment of grain boundary density), dislocations' density, the orientation of grains, residual stress, number of defects, passive film formation, etc. These factors can influence the electrochemical behavior of material and corrosion susceptibility, as mentioned in many studies [52–54]. Figure 6 and Table 3 show that the corrosion current ($i_{corr}$) decreases with the increment of the CEC pass number. This can be due to the facile formation of a protective oxide layer on the refined microstructures since the high density of grain boundaries can act as suitable nucleation sites for oxide layers. Additionally, Table 3 includes all the electrochemical parameters, and Figure 6 plots illustrate that the annealed state has more negative corrosion potential ($E_{corr}$) values than the CEC-processed sample indicating lower corrosion resistance, while the CEC-processed sample with more positive $E_{corr}$ values has lower corrosion rates. As it can be inferred from Figure 2 and Table 2, the CEC process leads to substantial grain refinement (from ~23 µm for the annealed sample to 0.8 µm in the four passes CECed sample), increment of HAGBs fraction, and dislocation density. These variations facilitate the generation of protective oxide layers due to higher stored energy magnitudes in the non-equilibrium grain boundaries and the presence of higher internal stresses, providing additional surface

area by dislocations and defects, which resulted in promoting the formation of a large fraction of the passive layer, and finally, the higher internal stresses provide the required driving forces [55,56]. Furthermore, Oskooie et al. [56] have evidenced that UFG structures fabricated thicker and stronger oxide films compared to coarse structures. To date, several studies have been performed on the corrosion resistance of SPD-processed metals and alloys. For instance, it has been concluded that the high passivity rate and low impurity separation at the grain boundaries are responsible for increasing the corrosion resistance in the UFG structures [57]. Regarding different SPD techniques and especially the ECAP process, it should be noted that some degree of microstructure heterogeneities, such as grain boundaries and dislocation density, can be a reason for different electrochemical properties observed in the results of previous reports [58,59].

After the potentiodynamic polarization test in 3.5% NaCl solution, all the corroded samples were examined under an SEM device to study the morphology of corrosion attack in the annealed and different passes of CECed samples. Pit formation can be detected in all the samples, which are simultaneously due to potential increment and electrochemical attack by $Cl^-$ ions of the NaCl solution. It is known that $Cl^-$ ion concentration can change the anodic current, pitting potential (Epit), and the corrosion rate of the samples. It can also break the protective oxide layers leading to a pitting corrosion attack [60]. The annealed sample has the most nonuniform surface condition with lots of large-sized and deep pitting, while CEC processing, along with the increment of pass numbers, leads to the formation of a more uniform oxide layer with less tendency toward pitting. As a result, CEC processing results in fewer pit numbers and sizes with a more uniform surface condition due to the generation of oxide films since it can be concluded that CEC processing and grain refinement can increase the resistance against pitting corrosion. As it can be inferred from the SEM micrographs of Figure 7, the annealed sample has many large-sized and deep pits with random distribution, while the four-passed sample has a quite uniform and flat surface with fewer and more shallow pits. It can be claimed that the UFG structure of CEC-processed samples with higher residual stresses (keeping the passive film stable) and non-equilibrium grain boundaries has more tendency toward the formation of protective oxide layers, thus manifesting higher resistance against pitting, sustaining the sample in aggressive chlorine environments [61,62]. The presented EDS results in Figure 8 indicate a considerable amount of oxygen and chlorine elements in both annealed and CEC-processed samples, confirming the presence of oxide films and chlorine attack. In addition, Figure 9 illustrates the (EDS) map analysis (elemental map) of the corrosion products with the distribution of oxygen all over the sample as an indicator for protective oxide layer formation. Additionally, it can be seen that Na and Cl elements are dispersed in a nonuniform condition, and they are presented predominantly in the periphery of pitting regions, which depicts the considerable role of salt and chlorine ions in the pitting occurrence, while other elements show a quite uniform condition. It can be concluded that these microscopy observations are in acceptable accordance with electrochemical polarization results and microstructural evolution.

The improved hardness behavior and enhanced corrosion resistance of the UFG Al5052 sample will expand the potential applications of this alloy in industries of marine, automobile, aircraft, and other vehicles. Its applications can also be extended to the conductors, instrument panels, lining plates of refrigerators, automobile gas pipes, oil pipes, agricultural irrigation pipes, aircraft fuel tanks, traffic vehicles, instrumentation, street lamp support and rivets, hardware products, agricultural insect traps, cryogenic equipment, TV tower, drilling equipment, transportation equipment, missile and deck parts, car body plates, control plates, strengthening parts, brackets, decorative parts, etc.
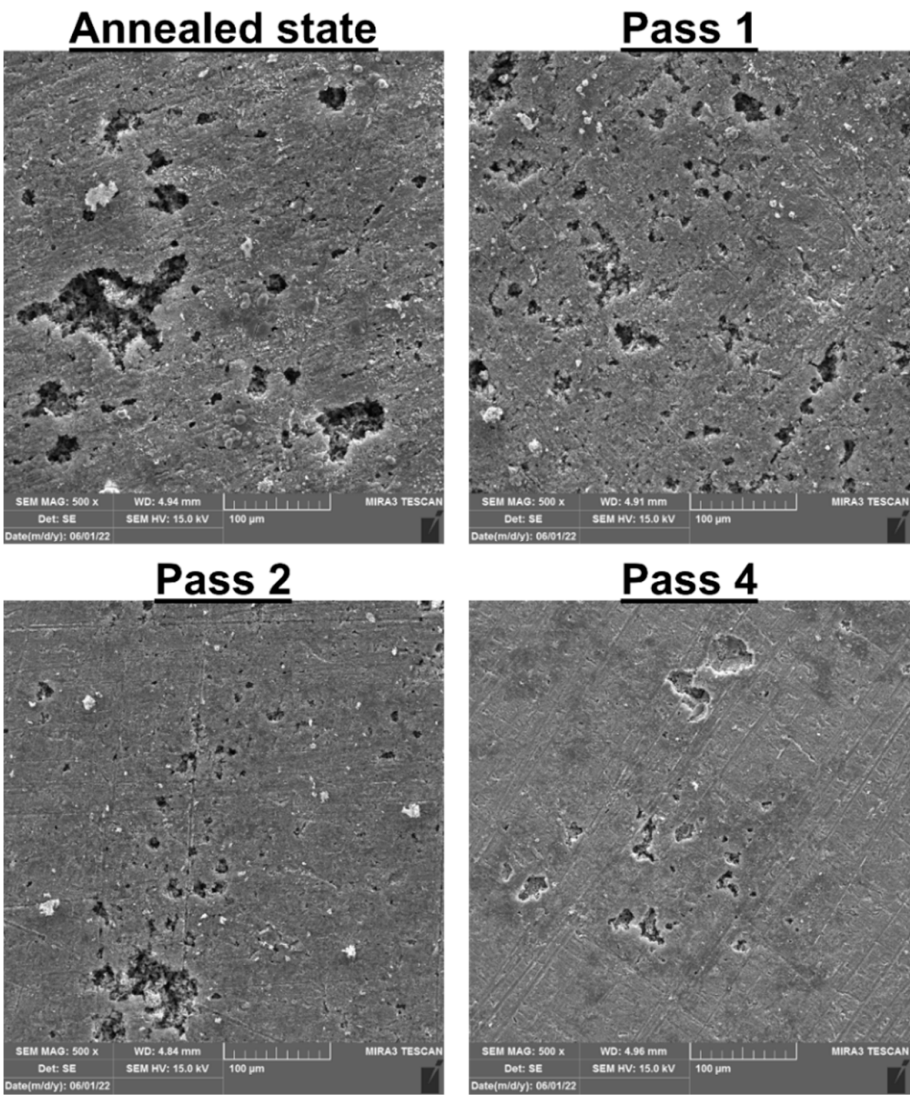
**Figure 7.** SEM micrographs of the corroded surface morphology after the potentiodynamic polarization test for the Al5052 sample before and after the CEC process at the different pass numbers up to four passes.
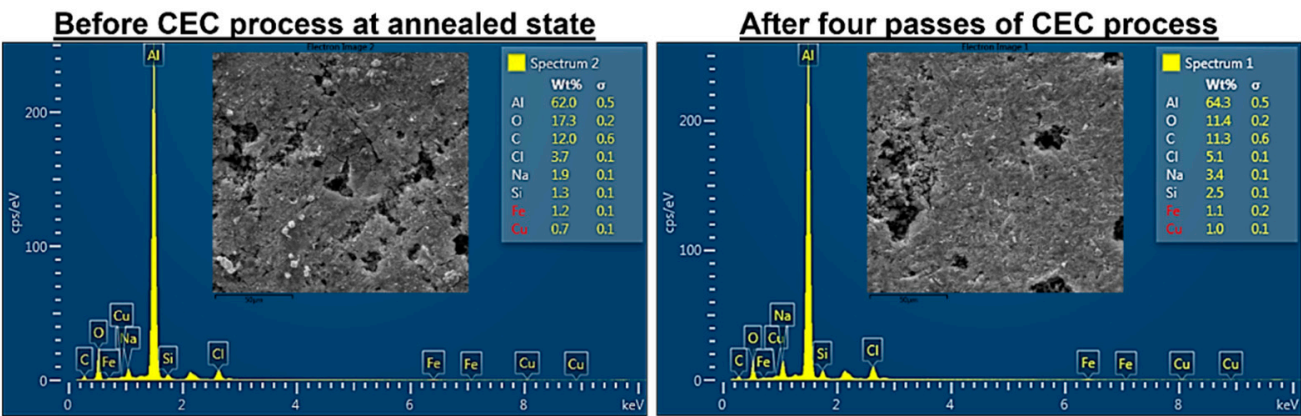


**Figure 8.** Energy dispersive spectroscopy (EDS) of the corrosion products in the Al5052 sample for the annealed state and final pass condition.
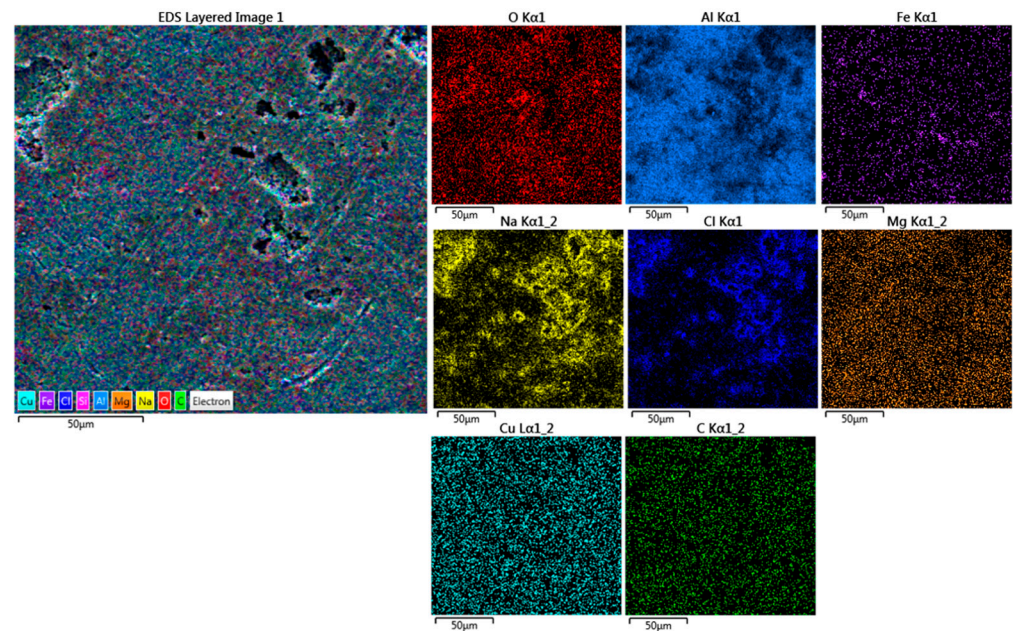
**Figure 9.** Energy dispersive spectroscopy (EDS) map analysis (elemental map) of the corrosion products after the potentiodynamic polarization test of the Al5052 sample in the four-pass CEC-processed sample.

## 4. Conclusions

The Al5052 alloy, as an important material class in engineering applications, should be improved from mechanical properties, microstructural conditions, and electrochemical behavior perspectives. In this study, CEC processing as a suitable severe plastic deformation method was used on Al5052 alloy up to four passes. Then, the resultant mechanical, microstructural, and corrosion resistance were studied to gain a full insight into its engineering performance. The significant results were attained as below:

- The extreme grain refinement was attained by CEC processing, which transforms the initial annealed and coarse-grained Al5052 sample with a mean grain size of ~23 μm into a UFG structure with an average grain size of ~0.8 μm after four passes of CEC;
- The occurrence of continuous dynamic recrystallization was the main reason for microstructural refinement leading to the increment of HAGBs during CEC processing. Another effective mechanism in the microstructural evolution of Al5052 alloy was geometric dynamic recrystallization;
- It was seen that the CEC technique led to an increment of hardness value and its homogeneity since the final pass CEC-processed alloy had the highest hardness value of 139.7 HV with the suitable dispersion uniformity (SD of 3.738);
- The CEC processing led to the improvement in corrosion resistance up to 45.5%, and the addition of pass number reduced the corrosion current density and the corrosion rate. The corrosion rate of the sample in the initial annealing state and after the first, second, and fourth passes were respectively equal to 1.489, 1.111, 1.055, and 1.023 mpy. In addition, the more negative corrosion potential of the annealed samples compared to CEC-processed samples indicated the improvement in corrosion resistance by CEC application and the addition of pass numbers;
- The improvement in corrosion resistance by CEC processing was related to the production of the protective oxide layer, which is more prone to produce on a higher fraction of grain boundaries and higher residual stresses of CEC-processed samples;
- The corroded surface of all the samples showed the formation of many pits, which is more large-sized and deeper in the initial state, and, subsequently, the number of these pits, size, and depth were reduced by CEC application. The pitting formation

was related to the presence of chlorine ions and increment of potential, which attacks the protective oxide layer.

## References

1. Staley, J.T.; Lege, D.J. Advances in Aluminium Alloy Products for Structural Applications in Transportation. *Le J. Phys. IV* **1993**, *03*, C7-170–C7-179. [CrossRef]
2. Cole, G.S.; Sherman, A.M. Light Weight Materials for Automotive Applications. *Mater. Charact.* **1995**, *35*, 3–9. [CrossRef]
3. Starke, E.A.; Staley, J.T. Application of Modern Aluminium Alloys to Aircraft. *Prog. Aerosp. Sci.* **1996**, *32*, 131–172.
4. Omidi Bidgoli, M.; Reza Kashyzadeh, K.; Rahimian Koloor, S.S.; Petru, M. Estimation of Critical Dimensions for the Crack and Pitting Corrosion Defects in the Oil Storage Tank Using Finite Element Method and Taguchi Approach. *Metals* **2020**, *10*, 1372. [CrossRef]
5. Swamy, P.K.; Mylaraiah, S.; Gowdru Chandrashekarappa, M.P.; Lakshmikanthan, A.; Pimenov, D.Y.; Giasin, K.; Krishna, M. Corrosion Behaviour of High-Strength Al 7005 Alloy and Its Composites Reinforced with Industrial Waste-Based Fly Ash and Glass Fibre: Comparison of Stir Cast and Extrusion Conditions. *Materials* **2021**, *14*, 3929. [CrossRef] [PubMed]
6. Miller, W.S.; Zhuang, L.; Bottema, J.; Wittebrood, A.J.; De Smet, P.; Haszler, A.; Vieregge, A. Recent Development in Aluminium Alloys for the Automotive Industry. *Mater. Sci. Eng. A* **2000**, *280*, 37–49. [CrossRef]
7. Attarilar, S.; Ebrahimi, M.; Hsieh, T.-H.; Uan, J.-Y.; Göde, C. An Insight into the Vibration-Assisted Rolling of AA5052 Aluminum Alloy: Tensile Strength, Deformation Microstructure, and Texture Evolution. *Mater. Sci. Eng. A* **2021**, *803*. [CrossRef]
8. Ebrahimi, M.; Par, M.A. Twenty-Year Uninterrupted Endeavor of Friction Stir Processing by Focusing on Copper and Its Alloys. *J. Alloys Compd.* **2019**, *781*, 1074–1090. [CrossRef]
9. Vinogradov, A.; Estrin, Y. Analytical and Numerical Approaches to Modelling Severe Plastic Deformation. *Prog. Mater. Sci.* **2018**, *95*, 172–242. [CrossRef]
10. Ebrahimi, M.; Djavanroodi, F. Experimental and Numerical Analyses of Pure Copper during ECFE Process as a Novel Severe Plastic Deformation Method. *Prog. Nat. Sci. Mater. Int.* **2014**, *24*, 68–74. [CrossRef]
11. Bagherpour, E.; Pardis, N.; Reihanian, M.; Ebrahimi, R. An Overview on Severe Plastic Deformation: Research Status, Techniques Classification, Microstructure Evolution, and Applications. *Int. J. Adv. Manuf. Technol.* **2019**, *100*, 1647–1694. [CrossRef]
12. Kim, J.H.; Hwang, S.K.; Im, Y.-T.; Son, I.-H.; Bae, C.M. High-Strength Bolt-Forming of Fine-Grained Aluminum Alloy 6061 with a Continuous Hybrid Process. *Mater. Sci. Eng. A* **2012**, *552*, 316–322. [CrossRef]
13. Sasaki, T.T.; Morris, R.A.; Thompson, G.B.; Syarif, Y.; Fox, D. Formation of Ultra-Fine Copper Grains in Copper-Clad Aluminum Wire. *Scr. Mater.* **2010**, *63*, 488–491. [CrossRef]
14. Djavanroodi, F.; Sedighi, M.; Hashemi, P.; Ebrahimi, M. Equal Channel Angular Pressing of Copper Wire. *Proc. Inst. Mech. Eng. Part B J. Eng. Manuf.* **2014**, *228*. [CrossRef]
15. Djavanroodi, F.; Zolfaghari, A.A.; Ebrahimi, M.; Nikbin, K.M. Equal Channel Angular Pressing of Tubular Samples. *Acta Metall. Sin.* **2013**, *26*, 574–580. [CrossRef]
16. Ebrahimi, M.; Attarilar, S.; Gode, C.; Djavanroodi, F. Damage Prediction of 7025 Aluminum Alloy during Equal-Channel Angular Pressing. *Int. J. Miner. Metall. Mater.* **2014**, *21*. [CrossRef]
17. Aal, M.I.A.E.; Kim, H.S. Wear Properties of High Pressure Torsion Processed Ultrafine Grained Al–7%Si Alloy. *Mater. Des.* **2014**, *53*, 373–382. [CrossRef]
18. Ansarian, I.; Shaeri, M.H.; Ebrahimi, M.; Minárik, P.; Bartha, K. Microstructure Evolution and Mechanical Behaviour of Severely Deformed Pure Titanium through Multi Directional Forging. *J. Alloys Compd.* **2019**, *776*. [CrossRef]
19. Ebrahimi, M.; Gholipour, H.; Djavanroodi, F. A Study on the Capability of Equal Channel Forward Extrusion Process. *Mater. Sci. Eng. A* **2015**, *650*, 1–7. [CrossRef]
20. Wang, Y.; Fu, R.; Jing, L.; Li, Y.; Sang, D. Grain Refinement and Nanostructure Formation in Pure Copper during Cryogenic Friction Stir Processing. *Mater. Sci. Eng. A* **2017**, *703*, 470–476. [CrossRef]
21. Fan, R.-J.; Attarilar, S.; Shamsborhan, M.; Ebrahimi, M.; Göde, C.; Özkavak, H.V. Enhancing Mechanical Properties and Corrosion Performance of AA6063 Aluminum Alloys through Constrained Groove Pressing Technique. *Trans. Nonferrous Met. Soc. China* **2020**, *30*, 1790–1802. [CrossRef]

22. Naeini, M.F.; Shariat, M.H.; Eizadjou, M. On the Chloride-Induced Pitting of Ultra Fine Grains 5052 Aluminum Alloy Produced by Accumulative Roll Bonding Process. *J. Alloys Compd.* **2011**, *509*, 4696–4700. [CrossRef]

23. Ebrahimi, M. Fatigue Behaviors of Materials Processed by Planar Twist Extrusion. *Metall. Mater. Trans. A* **2017**, *48*, 6126–6134. [CrossRef]

24. Ebrahimi, M.; Shamsborhan, M. Monotonic and Dynamic Mechanical Properties of PTCAE Aluminum. *J. Alloys Compd.* **2017**, *705*, 28–37. [CrossRef]

25. Wang, L.P.; Chen, T.; Jiang, W.Y.; Feng, Y.C.; Cao, G.J.; Zhu, Y. Microstructure and Mechanical Properties of AM60B Magnesium Alloy Prepared by Cyclic Extrusion Compression. *Trans. Nonferrous Met. Soc. China* **2013**, *23*, 3200–3205. [CrossRef]

26. Richert, M. The Effect of Unlimited Cumulation of Large Plastic Strains on the Structure-Softening Processes of 99.999 Al. *Mater. Sci. Eng. A* **1990**, *129*, 1–10. [CrossRef]

27. Zhang, L.; Wang, Q.; Liao, W.; Guo, W.; Li, W.; Jiang, H.; Ding, W. Microstructure and Mechanical Properties of the Carbon Nanotubes Reinforced AZ91D Magnesium Matrix Composites Processed by Cyclic Extrusion and Compression. *Mater. Sci. Eng. A* **2017**, *689*, 427–434. [CrossRef]

28. Chen, Y.J.; Wang, Q.D.; Lin, J.B.; Liu, M.P.; Hjelen, J.; Roven, H.J. Grain Refinement of Magnesium Alloys Processed by Severe Plastic Deformation. *Trans. Nonferrous Met. Soc. China* **2014**, *24*, 3747–3754. [CrossRef]

29. Sułkowski, B.; Janoska, M.; Boczkal, G.; Chulist, R.; Mroczkowski, M.; Pałka, P. The Effect of Severe Plastic Deformation on the Mg Properties after CEC Deformation. *J. Magnes. Alloy.* **2020**, *8*, 761–768. [CrossRef]

30. Segal, V.M. Deformation Mode and Plastic Flow in Ultra Fine Grained Metals. *Mater. Sci. Eng. A* **2005**, *406*, 205–216. [CrossRef]

31. Kaibyshev, R.; Malopheyev, S. Mechanisms of Dynamic Recrystallization in Aluminum Alloys. *Mater. Sci. Forum* **2014**, *794–796*, 784–789. [CrossRef]

32. McQueen, H.J. Distinguishing Dynamic Recrystallization (DRX) in Aluminum and Single-Phase Alloys. *ICAA13 Pittsburgh.* 2012, pp. 951–956. Available online: https://link.springer.com/chapter/10.1007/978-3-319-48761-8_143 (accessed on 30 May 2022).

33. Ajaoa, O.J.; Owolabib, G.M.; Whitworthc, H.A.; Scott-Emuakpor, O. Dynamic Impact Response of Ultrafine Grained AA5052 Aluminum Alloy Processed Via Multiaxial Forging at Cryogenic Temperature. *Turkish J. Comput. Math. Educ.* **2021**, *12*, 5082–5094. [CrossRef]

34. Ko, Y.G.; Hamad, K. Microstructure Stability and Mechanical Properties of Ultrafine Grained 5052 Al Alloy Fabricated by Differential Speed Rolling. *Mater. Sci. Eng. A* **2018**, *733*, 24–27. [CrossRef]

35. Mohebbi, M.S.; Akbarzadeh, A. Constitutive Equation and FEM Analysis of Incremental Cryo-Rolling of UFG AA 1050 and AA 5052. *J. Mater. Process. Technol.* **2018**, *255*, 35–46. [CrossRef]

36. Dai, K.; Villegas, J.; Stone, Z.; Shaw, L. Finite Element Modeling of the Surface Roughness of 5052 Al Alloy Subjected to a Surface Severe Plastic Deformation Process. *Acta Mater.* **2004**, *52*, 5771–5782. [CrossRef]

37. Dai, K.; Villegas, J.; Shaw, L. An Analytical Model of the Surface Roughness of an Aluminum Alloy Treated with a Surface Nanocrystallization and Hardening Process. *Scr. Mater.* **2005**, *52*, 259–263. [CrossRef]

38. Yagami, T.; Manabe, K.; Miyamoto, T. Ductile Fracture Behavior of 5052 Aluminum Alloy Sheet under Cyclic Plastic Deformation at Room Temperature. *J. Mater. Process. Technol.* **2009**, *209*, 1042–1047. [CrossRef]

39. Ui, G.G.; Sang, H.L.; Won, J.N. The Evolution of Microstructure and Mechanical Properties of a 5052 Aluminium Alloy by the Application of Cryogenic Rolling and Warm Rolling. *Mater. Trans.* **2009**, *50*, 82–86. [CrossRef]

40. Entezami, S.S.; Honarpisheh, M. A Study on the Hardness of 7075 and 5052 Aluminum Alloys in the Equal Channel Angular Rolling Process. *Bull. la Société R. des Sci. Liège* **2016**, *85*, 879–889. [CrossRef]

41. Song, P.; Li, W.B.; Wang, X.M. A Study on Dynamic Plastic Deformation Behavior of 5052 Aluminum Alloy. *Key Eng. Mater.* **2019**, *812 KEM*, 45–52. [CrossRef]

42. El-Garhy, G.; El Mahallawy, N.; Shoukry, M.K. Effect of Grain Refining by Cyclic Extrusion Compression (CEC) of Al-6061 and Al-6061/SiC on Wear Behavior. *J. Mater. Res. Technol.* **2021**, *12*, 1886–1897. [CrossRef]

43. Fundenberger, J.-J.; Beausir, B. Analysis Tools For Electron And X-Ray Diffraction. Available online: http://www.atex-software.eu/ (accessed on 30 May 2022).

44. Frint, P.; Härtel, M.; Selbmann, R.; Dietrich, D.; Bergmann, M.; Lampke, T.; Landgrebe, D.; Wagner, M. Microstructural Evolution during Severe Plastic Deformation by Gradation Extrusion. *Metals* **2018**, *8*, 96. [CrossRef]

45. Shaeri, M.H.; Shaeri, M.; Ebrahimi, M.; Salehi, M.T.; Seyyedein, S.H. Effect of ECAP Temperature on Microstructure and Mechanical Properties of Al-Zn-Mg-Cu Alloy. *Prog. Nat. Sci. Mater. Int.* **2016**, *26*. [CrossRef]

46. Yang, X.; Miura, H.; Sakai, T. Continuous Dynamic Recrystallization in a Superplastic 7075 Aluminum Alloy. *Mater. Trans.* **2002**, *43*, 2400–2407. [CrossRef]

47. Cao, J.; Sun, Z.; Wu, H.; Yin, Z.; Huang, L. Continuous Dynamic Recrystallization Prediction in Multi-Direction Loading Forming of 7075 Aluminum Alloy Tee Valve. *IOP Conf. Ser. Mater. Sci. Eng.* **2018**, *439*, 022015. [CrossRef]

48. Mogucheva, A.; Babich, E.; Ovsyannikov, B.; Kaibyshev, R. Microstructural Evolution in a 5024 Aluminum Alloy Processed by ECAP with and without Back Pressure. *Mater. Sci. Eng. A* **2013**, *560*, 178–192. [CrossRef]

49. Lv, J.; Zheng, J.H.; Yardley, V.A.; Shi, Z.; Lin, J. A Review of Microstructural Evolution and Modelling of Aluminium Alloys under Hot Forming Conditions. *Metals* **2020**, *10*, 1516. [CrossRef]

50. Wang, Y.; Jin, J.; Zhang, M.; Liu, F.; Wang, X.; Gong, P.; Tang, X. Influence of Plastic Deformation on the Corrosion Behavior of CrCoFeMnNi High Entropy Alloy. *J. Alloys Compd.* **2022**, *891*, 161822. [CrossRef]

51.  Abu Seman, A.; Chan, J.K.; Norazman, M.A.; Hussain, Z.; Brij, D.; Ismail, A. Corrosion Behavior of Heat-Treated and Cryorolled Al 5052 Alloys in Different Chloride Ion Concentrations. *Anti-Corrosion Methods Mater.* **2020**, *67*, 7–15. [CrossRef]

52.  Miyamoto, H. Corrosion of Ultrafine Grained Materials by Severe Plastic Deformation, an Overview. *Mater. Trans.* **2016**, *57*, 559–572. [CrossRef]

53.  Akiyama, E.; Zhang, Z.; Watanabe, Y.; Tsuzaki, K. Effects of Severe Plastic Deformation on the Corrosion Behavior of Aluminum Alloys. *J. Solid State Electrochem.* **2009**, *13*, 277–282. [CrossRef]

54.  Gode, C.; Attarilar, S.; Eghbali, B.; Ebrahimi, M. Electrochemical Behavior of Equal Channel Angular Pressed Titanium for Biomedical Application. *AIP Conf. Proc.* **2015**, *1653*, 020041.

55.  Wei, W.; Wei, K.X.; Du, Q.B. Corrosion and Tensile Behaviors of Ultra-Fine Grained Al–Mn Alloy Produced by Accumulative Roll Bonding. *Mater. Sci. Eng. A* **2007**, *454–455*, 536–541. [CrossRef]

56.  Shakoori Oskooie, M.; Asgharzadeh, H.; Sadighikia, S.; Salehi, M. Significant Corrosion Resistance in an Ultrafine-Grained Al6063 Alloy with a Bimodal Grain-Size Distribution through a Self-Anodic Protection Mechanism. *Metals* **2016**, *6*, 307. [CrossRef]

57.  Balyanov, A.; Kutnyakova, J.; Amirkhanova, N.A.; Stolyarov, V.V.; Valiev, R.Z.; Liao, X.Z.; Zhao, Y.H.; Jiang, Y.B.; Xu, H.F.; Lowe, T.C.; et al. Corrosion Resistance of Ultra Fine-Grained Ti. *Scr. Mater.* **2004**, *51*, 225–229. [CrossRef]

58.  Alfantazi, A.M.; Ahmed, T.M.; Tromans, D. Corrosion Behavior of Copper Alloys in Chloride Media. *Mater. Des.* **2009**, *30*, 2425–2430. [CrossRef]

59.  Nickel, D.; Dietrich, D.; Mehner, T.; Frint, P.; Spieler, D.; Lampke, T. Effect of Strain Localization on Pitting Corrosion of an AlMgSi0.5 Alloy. *Metals* **2015**, *5*, 172–191. [CrossRef]

60.  Desouky, H.E.; Aboeldahab, H.A. Effect of Chloride Concentration on the Corrosion Rate of Maraging Steel. *Open J. Phys. Chem.* **2014**, *04*, 147–165. [CrossRef]

61.  Rhouma, A.B.; Braham, C.; Fitzpatrick, M.E.; Leidion, J.; Sidhom, H. Effects of Surface Preparation on Pitting Resistance, Residual Stress, and Stress Corrosion Cracking in Austenitic Stainless Steels. *J. Mater. Eng. Perform.* **2001**, *10*, 507–514. [CrossRef]

62.  Ralston, K.D.; Birbilis, N. Effect of Grain Size on Corrosion: A Review. *Corrosion* **2010**, *66*, 075005. [CrossRef]